Hydrodynamics of median-fin interactions in fish-like locomotion: Effects of fin shape and movement Ⓢ Ⓕ

View Online   Export Citation   CrossMark

Pan Han (韩攀),[1] ⓘD George V. Lauder,[2] ⓘD and Haibo Dong (董海波)[1,a] ⓘD

AFFILIATIONS

[1] Department of Mechanical and Aerospace Engineering, University of Virginia, Charlottesville, Virginia 22904, USA

[2] Museum of Comparative Zoology and Department of Organismic and Evolutionary Biology, Harvard University, Cambridge, Massachusetts 02138, USA

[a] Author to whom correspondence should be addressed: haibo.dong@virginia.edu

ABSTRACT

Recent studies have shown that by utilizing the interactions among median fins (the dorsal, anal, and caudal fins), fishes can achieve higher propulsion performance at the caudal fin. This work aims at a systematic study of the effects of dorsal/anal fin shape and flapping phase on the hydrodynamic performance due to median-fin interactions (MFI) in underwater propulsion using a three-dimensional bluegill sunfish model. Flow simulations were conducted on stationary Cartesian grids using an immersed-boundary-method-based incompressible Navier-Stokes flow solver. The results showed that, due to the collision between the posterior body vortices (PBVs) and caudal fin leading edge vortices (LEVs), the latter is strengthened. As a result, the thrust and efficiency of the caudal fin are improved simultaneously, by 25.6% and 29.2%, respectively. Increases in the dorsal/anal fin area result in stronger caudal fin LEVs, and thus further caudal fin performance enhancement. On the other hand, changing the dorsal/anal fin flapping phase affects the collision time between the PBVs and the LEVs, and results in caudal fin performance changes. Phase-leading dorsal and anal fins are found to improve caudal fin efficiency, whereas phase-lag dorsal and anal fins maintain caudal fin thrust at a higher level. Compared to trunk-synchronized dorsal and anal fins, 60° phase-leading dorsal and anal fins increase the propulsive efficiency of the caudal fin from 77.9% to 90.1%. In addition, it is found that the presence of the dorsal and anal fins greatly reduces drag on the fish body by preventing the PBVs from crossing the body midline and debilitating interactions between the left- and right-stroke PBVs. Results of this work improve our understanding of MFI in fishlike swimming and demonstrate the benefits of optimal MFI for the design of high-performance bioinspired underwater vehicles.

Published under license by AIP Publishing. https://doi.org/10.1063/1.5129274

I. INTRODUCTION

One hallmark of fish swimming is the coordination between body undulation and motion of median fins, such as the dorsal, anal, and caudal fins.[1,2] Previous research[3,4] has suggested that flow shed by the dorsal and anal fins could potentially enhance the propulsive performance of the caudal fin. With experimental and numerical methods, Wolfgang *et al.* studied the flow pattern of giant danio (*Danio malabaricus*) and found that the caudal fin constructively interacts with the body-generated vortex in fish straight-line swimming.[5] Using particle imaging velocimetry (PIV) measurements, Drucker and Lauder have observed the wake interactions between the upstream dorsal fin and downstream caudal fin of teleost fish such as bluegill sunfish (*Lepomis macrochirus*)[6] and rainbow trout

(*Oncorhynchus mykiss*),[7] and hypothesized that the caudal fin could intercept vortices shed periodically from dorsal and anal fins to enhance its thrust. Tytell[8] later analyzed the three-dimensional (3D) streamwise vortex structures of bluegill sunfish and proposed that the caudal fin could angle itself correctly to take advantage of these wake interactions and thus enhance thrust. Similar conclusions were also made from studies in brook trout (*Salvelinus fontinalis*) by Standen and Lauder,[9] based on the observation of the caudal fin passing through the incident flow induced by the dorsal and anal fins located upstream.

Using direct numerical simulations (DNS), Liu *et al.*[10] quantitatively investigated the 3D body-fin and fin-fin interactions in Crevalle Jack (*Caranx hippos*) fish, and confirmed previous hypotheses of fin-fin interactions. By extracting energy from

vortices shed from the dorsal and anal fins, the leading edge vortices (LEVs) on the caudal fin, which is closely related to the caudal fin pressure distribution,[11] are significantly strengthened and up to a 13.4% increase in caudal fin thrust was achieved in Crevalle Jack. In addition, the dorsal and anal fins reduced body drag (by about 20%) by giving rise to a larger pressure difference between the opposite sides of the fish body. More recently, Zhong *et al.*[12] have studied the effects of the dorsal fin sharpness on the swimming speed and economy with a tuna-inspired fish model, and found that, similar to the wing strakes of the fixed-wing aircraft, the dorsal-fin-induced cross-flow stabilizes the leading edge vortex of the caudal fin and thus improves its hydrodynamic performance.

Although considerable progress has been made in the study of fin-fin interactions in fishes, analysis of dorsal and anal fins' effects on propulsive performance in teleost fishes remains limited to two areas owing to the soft, flexible fin rays that comprise the fin surfaces.[2,13] First, studies on the kinematics of largemouth bass (*Micropterus salmoides*),[14] yellow perch (*Perca flavescens*),[15] rainbow trout (*Oncorhynchus mykiss fontinalis*),[7] and bluegill sunfish[16] showed that, during steady swimming, the teleost fishes are able to adjust the height of their dorsal and anal fins at different swimming speeds. Moreover, the changes of the dorsal fin shape due to fin damage caused by aggressive attacks between fish[17] and fish welfare issues[18,19] have been reported. MacLean *et al.*[17] have observed that 130 out of 139 juvenile Atlantic salmon lost 10%–40% of their dorsal fin tissue as a result of the aggression behavior. Though a recent study on biorobotic fish[14] has shown that, compared to the folded fin state, fully erected dorsal and anal fins increase the linear acceleration rate of the robotic fish model by as much as 32.5%, the effects of the dorsal and anal fin area on the fish steady swimming still need to be explored. Second, due to fin ray flexibility, the dorsal and anal fins are found oscillating out of phase with respect to the body trunk[16] and caudal fin. Standen and Lauder[16] looked into the three-dimensional (3D) fin kinematics of a swimming bluegill sunfish and found that, during propulsion, though the dorsal and

anal fins are oscillating in phase, between the trunk and dorsal/anal fin, an obvious phase-shift exists. In an earlier work,[6] in comparison with the movement of the caudal fin, phase-advanced dorsal fin motion was observed in bluegill sunfish. These results suggest that, rather than simply following the motion of the trunk with in-phase movements, the partially phase-independent motions of the dorsal and anal fins might play more complex roles in fish propulsion. In addition, both computational and experimental studies of idealized two-dimensional hydrofoils have suggested that, by optimizing the phase offset and relative position between hydrofoils, propulsors can improve performance by operating in close proximity.[20–26]

In this paper, a 3D model of bluegill sunfish with flexible dorsal and anal fins was employed to systematically investigate the shape and flapping phase effects of dorsal and anal fins on median-fin interaction (MFI). Using an in-house high-fidelity computational fluid dynamics (CFD) solver, 3D flow structures of the fish model were studied first. Then, subsequent simulations changing the dorsal/anal fin shape and flapping phase were conducted. By comparing the thrust force and propulsive efficiency between different cases, the benefits of MFI were studied quantitatively. Further analysis of vortex dynamics and surface pressure distributions were performed to elucidate the underlying mechanisms of the MFI.

The current paper is organized as follows. In Sec. II, the physical problem is presented, including the sunfish-like model with key geometric parameters and the kinematics description. The numerical method and simulation setup are then given in Sec. III. In Sec. IV, the simulation results are discussed in the context of hydrodynamic performance and vortex dynamics. Conclusions are summarized in Sec. V.

II. BLUEGILL SUNFISH-LIKE BODY-FIN MODEL AND PROBLEM DEFINITION

In this paper, a 3D bluegill sunfish trunk-fin model, including the body trunk (TK), dorsal fin (DF), anal fin (AF), and caudal fin (CF), is employed, as shown in Fig. 1(a). Similar to the previous
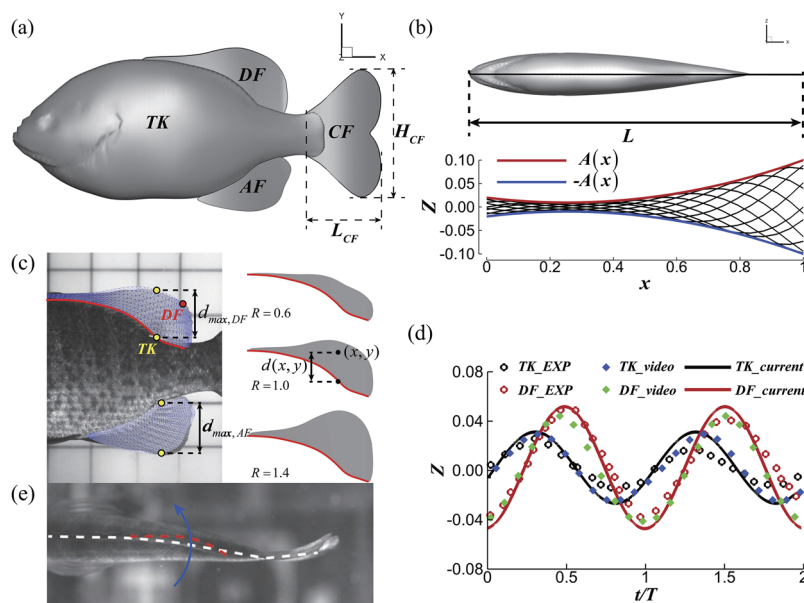

FIG. 1. (a) Lateral view of the bluegill sunfish-like model. (b) Midlines of the bluegill sunfish-like model during undulatory motion. (c) Comparison of the dorsal and anal fin geometries with natural shapes, and samples of dorsal fin shapes with different R values seen in the side view. The red lines delineate the base edge of the dorsal fin, which conforms to the trunk and remains unchanged when R is changing. (d) Comparison of the trunk and dorsal fin lateral excursions between the current undulatory kinematics ($R = 1.0$, $\varphi = 20°$) and the kinematic data digitized from video recordings and previous experimental results[16] (EXP) of bluegill sunfish swimming at 2.0 L/s. (e) A top view snapshot of a bluegill sunfish individual swimming at 2.0 L/s. The body midline and the dorsal fin outer edge are delineated by the dashed white and red lines, respectively.

work of Liu *et al.*,[10] a solid body with a closed surface is used to model the TK, and membranous plates are used to model the fins. Key geometric and kinematics quantities associated with this model are defined in Fig. 1(b), where L denotes the total body length, and $A(x)$ describes the lateral excursion envelope of the trunk and fins.

Fin morphology and body kinematic data were obtained from bluegill sunfish (mean total body length $\approx$16 cm) swimming in a recirculating flow tank (28 cm wide, 28 cm deep, 80 cm long) as in our previous research.[27,28] Three synchronized high-speed video cameras (Photron Fastcam and APX, Photron, Inc.) were used to record images at 500 Hz from the lateral (side), dorsal (top), and ventral (bottom) views. With these videos and the 3D surface reconstruction technology,[29] the deformation and motion of the body and fins were digitized simultaneously. Data on steady undulatory body locomotion was obtained at different speeds ranging from 0.5 body lengths/sec (L/s) to 2.5 L/s, and the fin geometry considered here is based on that of a fish swimming at 2.0 L/s. In Table I, the detailed geometric information is provided on the surface areas of the dorsal (S_{DF}), anal (S_{AF}), and caudal (S_{CF}) fins, maximum stretching heights

TABLE I. Geometric quantities of the bluegill sunfish model. (All the quantities in length scale and area scale are normalized by L and L^2, respectively.)

S_{DF}	S_{AF}	S_{CF}	$d_{max,DF}$	$d_{max,AF}$	L_{CF}	L_{CF}
0.028	0.020	0.050	0.142	0.133	0.346	0.205

of the dorsal fin ($d_{max,DF}$) and anal fin ($d_{max,AF}$), as well as the vertical height (H_{CF}) and streamwise length (L_{CF}) of the caudal fin. In the current model, the total area of dorsal and anal fins is very much comparable to that of the caudal fin. The maximum stretching height, which defines the largest vertical distance between the dorsal (anal) fin outer edge and the trunk, has a similar value for dorsal and anal fins.

To describe the undulatory motion of the swimming fish, similar to the previous work,[30] traveling wave equations with several key parameters are introduced as follows:

$$Z(x,y,t) = \begin{cases} A(x) \cdot \sin\left(\dfrac{2\pi}{\lambda}x - \dfrac{2\pi}{T}t\right), & \text{trunk/caudal fin,} \quad (1) \\[2em] \left(A(x) + A_{d_{max}}\dfrac{d(x,y)}{d_{max}}\right) \cdot \sin\left(\dfrac{2\pi}{\lambda}x - \dfrac{2\pi}{T}t + \varphi\dfrac{d(x,y)}{d_{max}}\right), & \text{dorsal/anal fin,} \quad (2) \end{cases}$$

$$A(x) = a_2 x^2 + a_1 x + a_0, \quad (3)$$

where all the quantities in the length scale are normalized by L. $Z(x, y, t)$ defines the lateral excursion of different body parts. x is the axial distance from the snout along the longitudinal direction; t is time and T is the period time, which has been normalized to be 1.0. λ is the wavelength, whose value has been observed to change among different swimming modes,[31] different swimming individuals using same mode,[32] and even the same individuals at different swimming speeds.[33,34] However, in the current work, to focus on the dorsal/anal fin shape and phase effects, the wavelength λ is fixed to be 1.0L, which is in the range of 0.89–1.10L observed in most carangiform swimmers.[35] $A(x)$ is denoted by a quadratic polynomial function in Eq. (3), with parameters $a_0 = 0.02$, $a_1 = -0.08$, and $a_2 = 0.16$, which were used for carangiform swimmers.[30] Figure 1(b) shows a sequence of midlines of the current fish model during one tail-beat cycle. Though the dorsal and anal fins are much smaller than the caudal fin in size and might have higher harmonics as elastic structures, in our current study, they are restricted to have a same flapping frequency with the caudal fin and their kinematics is described in Eq. (2). In Eq. (2), to define the lateral excursion and phase difference of the dorsal and anal fins with respect to the motion of the body trunk, two linear terms containing $A_{d_{max}}$ and φ are introduced, where $A_{d_{max}}$ is set to be 0.02L based on the previous work[16] and φ varies from $-100°$ (phase lead) to $100°$ (phase lag).

$d(x, y)$ defines the vertical distance between the dorsal (anal) fin point (x, y) and the dorsal (anal) fin base, where the local minimum (maximum) y value, $y_{min}|_x$ ($y_{min}|_x$), is achieved for the dorsal (anal) fin. d_{max} defines the maximum $d(x, y)$, as shown in Fig. 1(c). In addition, the dorsal and anal fins in our current computational model have d_{max} values of 0.142L and 0.133L, respectively. Furthermore, R is introduced as a shape factor to describe the dorsal/anal fin shape changes. In Fig. 1(c), $R = 1.0$ defines the natural dorsal/anal fin shape obtained from the high-speed videos at 2.0 L/s. With the edge of the dorsal/anal fin attaching to the trunk part (the base of the dorsal/anal fin) fixed, compressing or expanding the fin height by different factors R yields different dorsal/anal fin shapes, as shown in Fig. 1(c), where two additional dorsal fin shapes are presented and the fixed dorsal fin base edge is delineated by the red solid line. For simplicity, in all the simulations, the anal fin adopts same shape factor R with the dorsal fin. Due to the body conforming base edge of the dorsal and anal fins, the area of the dorsal and anal fins changes with the fin height with the same shape factor R.

To validate the current kinematic model in Fig. 1(d), the lateral excursions of two selected points on the body trunk ($x = 0.62$) and the dorsal fin edge ($x = 0.72$) [points TK and DF in Fig. 1(c)] are plotted, which show good agreement with the kinematic data digitized from video recordings and previous experimental data[16] of bluegill sunfish swimming at 2.0 L/s.
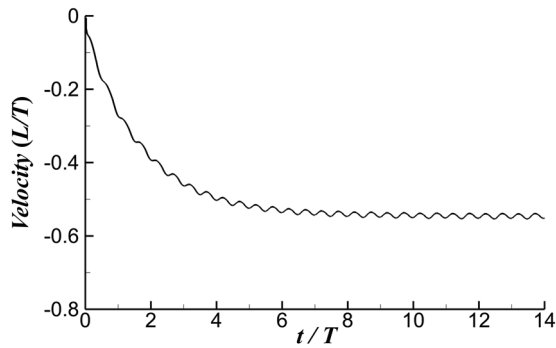
FIG. 2. The velocity of the free-swimming bluegill sunfish model center of mass as a function of time.

From the high-speed videos we took, we also observed that, some bluegill sunfish individuals employed phase-leading dorsal and anal fins during steady swimming. Figure 1(e) shows a snapshot of sunfish at 2.0 L/s. The body midline and dorsal fin outer edge were delineated by the dashed white and red lines. At this time instant, though the tail tip was moving downwards, the posterior trunk part started to flap upwards already, as denoted by the blue arrow. The dorsal fin presented a significant phase lead with respect to the trunk in this figure.

To examine the hydrodynamics of bluegill sunfish swimming, two key dimensionless parameters, the Strouhal number (St) and Reynolds number (Re), are denoted as follows:

$$St = \frac{f \cdot 2A_{CF}}{U_\infty}, \quad Re = \frac{U_\infty \cdot L}{\nu},$$

where f is the flapping frequency of the caudal fin, A_{CF} is the semi-amplitude of the caudal fin, U_∞ is the velocity of the incoming flow and ν is the kinematic viscosity. Although the Reynolds number of swimming bluegill sunfish is in the order of 10^4, it is always a challenge to do direct numerical simulations at such a high Reynolds number due to the current computational capability. In this study, a Reynolds number of 3000 is adopted according to the previous work of Liu et al.,[10] which showed that, above this Reynolds number, the fish swimming is still inertia-dominated and the MFI results do not change substantially. To choose the St for studying the MFI,

a self-propelled fish model with $R = 1.0$ and $\varphi = 0°$ is used to determine the U_∞ by restricting the degree of freedom of the fish swimming in the streamwise direction only. The time history of the center of mass streamwise velocity is plotted in Fig. 2. It shows that after about 10 cycles, the swimming speed of the fish model reaches a periodic state and the cycle-averaged speed is found to be 0.54 L/T, which corresponds to 0.37 Strouhal number used in the current study. This falls within the range of efficient fish propulsion.[36,37]

The surface pressure and shear force on the fish model's trunk and fins are projected from the flow variables around the fish body and integrated to compute the forces. In addition, the hydrodynamic power (P) is calculated from the integration along the model surface using $P = \oint -(\boldsymbol{\sigma} \cdot \boldsymbol{n}) \cdot \boldsymbol{V} ds$, where $\boldsymbol{\sigma}$ and $\boldsymbol{V}$ represent the stress tensor and the velocity vector of the fluid, and $\boldsymbol{n}$ is the normal vector of each point on the model surface. Two nondimensional coefficients (C_T and C_P) are defined to represent the thrust force (T) and the hydrodynamic power (P) as follows:

$$C_T = \frac{T}{0.5\rho U_\infty^2 S_{CF}}, \quad C_P = \frac{P}{0.5\rho U_\infty^3 S_{CF}},$$

where ρ is the fluid density and S_{CF} is the caudal fin area. Accordingly, the cycle-averaged thrust and power coefficients are denoted by $\overline{C}_T$ and $\overline{C}_P$, respectively. The hydrodynamic efficiency η is defined as the thrust-to-power ratio $(\overline{C}_T/\overline{C}_P)$. These parameters are used to compare the performance between different models in the following sections.

III. NUMERICAL METHOD AND SIMULATIONS

The 3D incompressible Navier-Stokes equations are employed as the governing equations and solved using an immersed-boundary-method based in-house CFD solver, which has been successfully applied in many simulations of flapping propulsion.[38–41] Details about this method can be found in Dong et al.[42] and validations about this solver can be found in our previous papers.[43]

Figure 3(a) shows a schematic of the nonuniform Cartesian grid employed in this paper, with a domain size chosen to be 10.0L × 6.0L × 6.0L. To resolve the trunk/fin shapes of the fish model and near-field vortex structures, a refined region of 1.2L × 0.6L
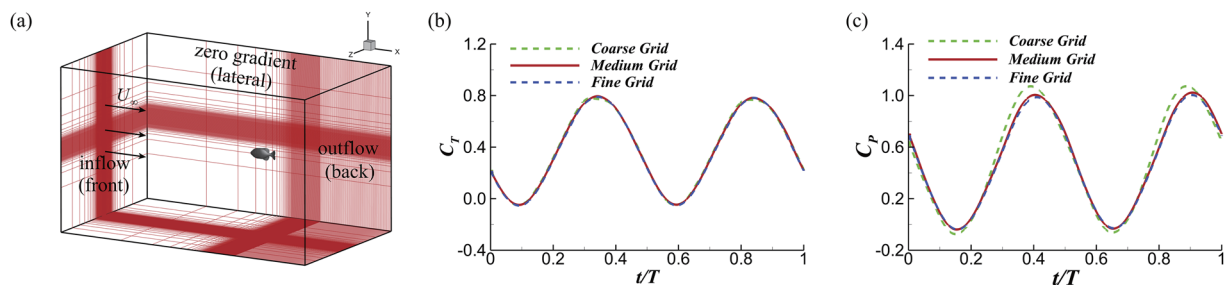

FIG. 3. (a) Schematic of the computational mesh and boundary conditions employed in this paper. Grid independent study on the caudal fin thrust (b) and caudal fin power (c) with three different grids, the coarse grid (305 × 121 × 153 ≈ 5.6 million, Δ_{min} = 0.0075L), the medium grid (385 × 193 × 193 ≈ 14.3 million, Δ_{min} = 0.0038L), and the fine grid (449 × 257 × 225 ≈ 26.0 million, Δ_{min} = 0.0025L).

TABLE II. Grid independent study results demonstrated the performance of the caudal fin.

Grid	Mean thrust $(\overline{C}_T)$	RMS thrust $(C_{T,RMS})$	Mean power $(\overline{C}_P)$	RMS power $(C_{P,RMS})$
Coarse	0.375	0.476	0.504	0.643
Medium	0.383	0.483	0.492	0.615
Fine	0.385	0.484	0.482	0.602

$\times 0.3L$ is set around the fish model. At the upstream boundary, a constant velocity incoming flow boundary condition is provided. At the downstream boundary, an outflow boundary condition is provided, allowing the vortices to convect out of this boundary without reflections. In addition, at all the lateral boundaries, the zero-gradient boundary condition is applied. For the pressure at all boundaries, a homogeneous Neumann boundary condition is applied.

To preclude grid dependence of the simulations, a grid independent study is conducted on three different grids (i.e., the coarse, medium, and fine grids). Figures 3(b) and 3(c) compare the corresponding instantaneous caudal fin thrust and power coefficients and show that, between the medium and fine grid, the difference in the peak thrust value is less than 1% and that in the peak power value is less than 2.0%. Table II compares the mean and root mean square (rms) values of the caudal fin thrust and power coefficients among grids. For all the values, the percentage differences show a magnitude less than 2.5% between the medium and fine grids. Therefore, the grid dependence of the hydrodynamic performance in the current study is excluded. For all the simulations below, the medium grid is employed.

IV. RESULTS AND DISCUSSION

In this section, the full trunk-fin model, which contains trunk and three median fins, with $R = 1.0$ and $\varphi = 0°$, is employed as the baseline case and its performance is discussed first. Then, the thrust and propulsive efficiency of the caudal fin are compared among models with different dorsal and anal fin shapes. The effects of phase difference between the upstream dorsal/anal fins and downstream caudal fin on the caudal fin performance are also studied. In addition, in the end, the effects of dorsal/anal fins on the trunk drag are investigated.

A. Hydrodynamic forces and wake topology of full trunk-fin model

In all simulations, to achieve periodic states, at least five undulatory cycles are simulated. Figure 4 shows the periodic hydrodynamic performance results of the full trunk-fin model with $R = 1.0$ and $\varphi = 0°$, where the subscript "1" in $C_{T,1}$ and $C_{P,1}$ denotes the baseline case. Figure 4(a) shows that, for all four parts included in the model, the trunk generates most of the drag force D, which is negative T, while the caudal fin works as the main propulsor. Compared to the caudal fin, the magnitude of forces generated by the dorsal and anal fins is much smaller. The instantaneous hydrodynamic power consumption of different parts is shown in Fig. 4(b), which shows that most of the power is consumed by the trunk and caudal fin. As the main propulsor, the $C_{P,1}$ amplitude of the caudal fin is much larger than that of the body trunk. Power consumption of the dorsal and anal fins is relatively small when compared to that of the trunk and caudal fin. In Table III, the $\overline{C}_{T,1}$ and $\overline{C}_{P,1}$ of different body parts are provided. The total force generated by the dorsal and anal fins is about 5% of the caudal fin force, which suggests lower hydrodynamic benefits of the dorsal and anal fins as propulsors.

Figures 5(a) and 5(b) show the 3D wake topology of the baseline case when the caudal fin just reaches its leftmost position and starts to move back to the opposite side. Due to the flapping motion, two sets of interconnected vortex rings are generated in the downstream region, which is consistent with the double row wake structures described in previous papers.[10,30] As observed in Fig. 5, vortices are generated in the posterior region of the body, especially at the outer and trailing edges of the dorsal and anal fins [terminology for these regions is based on Fig. 1(e) in Tytell[8]]. These vortices are denoted as posterior body vortices (PBVs) in Fig. 5(b). In Fig. 5(b), vortices generated by the leading edge and trailing edge of the caudal fin are denoted as LEV and TEV, respectively. Three slices are cut along the streamwise direction of the fish model and 2D streamwise vorticity contours are plotted in Figs. 5(c)–5(e) to compare with the experimental measurements by Tytell[8] at similar locations. Figure 5(c) shows the flow field at the trailing edge of the dorsal and anal fins. These two vortices labeled as "PBV" refer to the "dorsal fin" and "anal fin" vortices in Fig. 4(b) of Tytell.[8] Figure 5(e) shows the flow field at the posterior margin of the caudal fin. Comparison to Fig. 4(a) in Tytell[8] shows that vortices generated by the caudal fin tip and caudal fin notch, as well as the remnants of the dorsal and anal fin vortices, are similar in location and sign between the simulation and experiment.
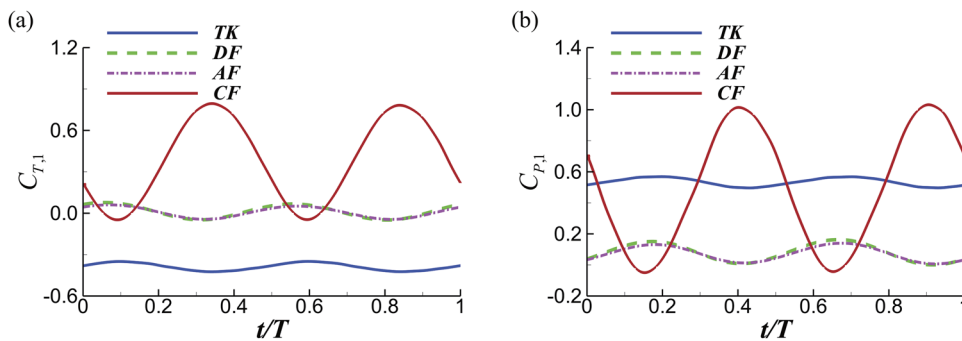

FIG. 4. (a) Thrust and (b) power coefficients generated by TK, DF, AF, and CF of the full trunk-fin model with $R = 1.0$ and $\varphi = 0°$ during one undulatory cycle.

TABLE III. Cycle-averaged thrust $\left(\overline{C}_{T,1}\right)$ and power coefficients $\left(\overline{C}_{P,1}\right)$ generated by different parts of the full trunk-fin model with $R = 1.0$ and $\varphi = 0°$.

	TK	DF	AF	CF
$\overline{C}_{T,1}$	−0.388	0.013	0.007	0.383
$\overline{C}_{P,1}$	0.534	0.082	0.073	0.492

B. Effects of dorsal and anal fin shape

To provide a comprehensive picture of how dorsal and anal fins affect the propulsive performance of the downstream caudal fin, computational models with different dorsal and anal fin shapes are employed to conduct simulations, with the phase difference φ fixed initially to $0°$.

In Fig. 6(a), cycle-averaged thrust coefficients $\overline{C}_T$ and efficiency η of the caudal fin are normalized by the baseline case and plotted with respect to the shape factor R. The simulation results indicate that, with the increase of the dorsal and anal fin area, the thrust generated by the caudal fin increases monotonously, though the rate of increase becomes smaller when $R > 1.0$. The normalized propulsive efficiency in Fig. 6(a) shares the same trend as that of the normalized thrust, which implies that, for all these simulations, the hydrodynamic power consumed by the caudal fin does not change much. When compared to the trunk-caudal fin only case ($R = 0.0$), the thrust and efficiency of case $R = 1.0$ are improved by 25.6% and 29.2%, respectively. Figure 6(b) shows a comparison of caudal fin thrust between four different models with $R = 0.0, 0.4, 1.0$, and 1.4. In general, the instantaneous force histories of all these four cases show two maxima for each stroke due to the flapping motion of the caudal fin. However, with the increase of the dorsal and anal fin area, the thrust generated by the caudal fin is improved during most of the

cycle. We also observed that increasing the dorsal and anal fin area makes the maximum thrust occur earlier in the flapping cycle. For instance, the maximum thrust is brought forward from $t/T = 0.90$ to $t/T = 0.84$, when R is increased from 0.0 to 1.0.

To understand the underlying mechanisms of this performance enhancement, we examine the vortex dynamics. Figure 7 shows instantaneous wake structures of models with different dorsal/anal fin shapes {$R = 0.0$ [(a1) and (a2)], $R = 0.4$ [(b1) and (b2)] and $R = 1.0$ [(c1) and (c2)]}, at the time instants $t/T = 0.58$ [(a1), (b1), and (c1)] and $t/T = 0.83$ [(a2), (b2), and (c2)], during which time the caudal fin of model $R = 1.0$, $\varphi = 0°$ produces dramatically more thrust than the other two cases. In Figs. 7(a1), 7(b1), and 7(c1), the caudal fin just reaches its leftmost position and then moves rightward in Figs. 7(a2), 7(b2), and 7(c2). The subscripts "R" and "L" represent the vortices generated in the rightward and leftward strokes, respectively. In Figs. 7(b1) and 7(c1), strong posterior body vortices (PBV_R) are found rolling up along the outer and trailing edges of the dorsal fin. As the dorsal fin moves rightward, the PBV_R in Figs. 7(b1) and 7(c1) sheds into the wake and collides with the leading edge vortex (LEV) of the caudal fin in Figs. 7(b2) and 7(c2). In Fig. 7(c2), a zoomed-in view is presented to show the detailed PBV_R and LEV collision. To implement a straightforward comparison, Figs. 7(a1) and 7(a2) show the wake structures of the trunk-caudal fin only model at the same time instants. It can be seen that, without the dorsal and anal fins, though PBV_R can still be generated along the dorsal and ventral edges of the trunk in Fig. 7(a1), flow is compressed toward the peduncle region and convects along the surface of the posterior trunk. Consequently, the collision between PBV_R and LEV does not happen in Fig. 7(a2), and thus the LEV generated at the caudal fin is weaker than that of the other two cases. The 3D wake structure results here indicate that the presence of the dorsal and anal fins enhances the propulsion performance of the caudal fin by inducing a stronger caudal fin LEV.
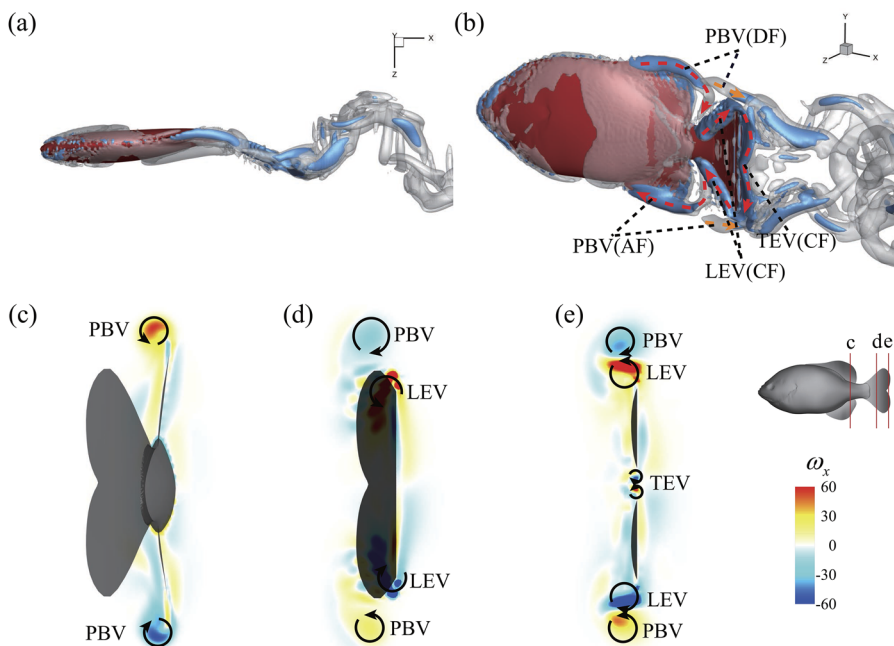

(a) (b) (c) (d) (e)

FIG. 5. Three-dimensional wake structure of the full trunk-fin bluegill sunfish model with $R = 1.0$ and $\varphi = 0°$ from the top view (a) and the perspective view (b). The wake structure is colored by the isosurface of Q-criterion. The isosurface $Q = 5$ is in grey and $Q = 40$ is in blue. The latter highlights the vortex core. Arrows in (b) indicate directionality of the vortex tubes or vortex rings. The red and orange arrows indicate vortices generated during right and left strokes, respectively. 2D streamwise vorticity contours are plotted at three cross section locations: the dorsal/anal fin trailing edge (c), the middle (d), and the posterior margin (e) of the caudal fin. The vorticity is normalized by U_∞/L.
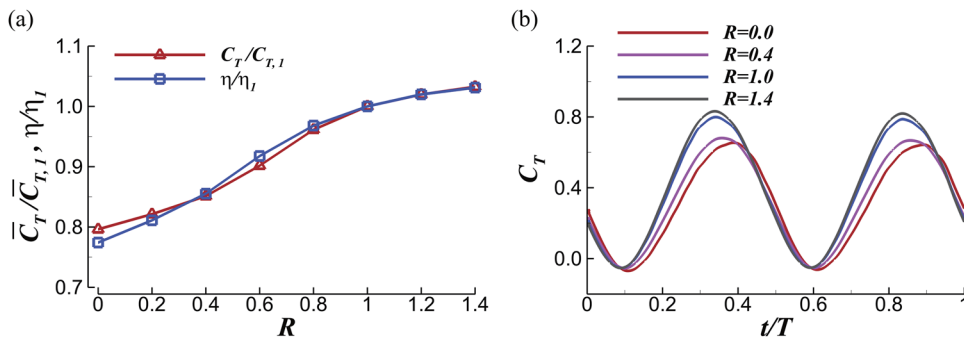
FIG. 6. (a) Cycle-averaged thrust coefficients ($\overline{C}_T$) and propulsive efficiency (η) of the caudal fin normalized with respect to the baseline case, whose cycle-averaged thrust coefficient and efficiency are denoted by $\overline{C}_{T,1}$ and η_1, respectively. (b) Instantaneous caudal fin thrust coefficients during one representative tail beat.

To better illustrate the interactions between the PBVs and the LEV, horizontal slices cutting the flow fields in Fig. 7 are plotted in Fig. 8 to show the contours of spanwise vorticity ω_y at the leading edge of the caudal fin. In Figs. 8(b1) and 8(c1), the clockwise vorticity ω_y of PBV_R is observed at the trailing edge of the dorsal fin and is about to convect into the downstream wake, whereas at this point, only a small PBV_R vorticity structure is found in Fig. 8(a1) at the dorsal edge of the trunk. After shedding from the trailing edge of the dorsal fin, the PBV_R in Figs. 8(b1) and 8(c1) propagates downstream and an interaction between PBV_R and LEV can be observed in Figs. 8(b2) and 8(c2). We observed that, due to the smaller streamwise distance between the dorsal fin and caudal fin in Figs. 8(b1) and 8(c1), the PBV_R maintains its strength before colliding with the LEV of the caudal fin. In addition, when $R = 1.0$, the PBV_R generated by the dorsal fin is much stronger than that of the case $R = 0.4$. However, at the same instant, in Fig. 8(a2), in this horizontal slice, the ω_y of the PBV_R is not observed. Referring back to Fig. 7(a2), the motion of PBV_R toward the peduncle region is considered as the reason why the clockwise PBV_R vorticity in Figs. 8(b2) and 8(c2) is not observed in Fig. 8(a2).

Circulation of the LEV is quantified during half stroke in Fig. 9 to compare the LEV strength among different cases. After the vorticity field is visualized and each vortex is identified, a closed contour

line with 20% of the maximum vorticity value is set around the LEV and the circulation is computed along this contour line. Figure 9(a) shows the comparison of LEV circulations at the slice, which is perpendicular to the leading edge of the caudal fin at its mid-span. It is found that, when $t/T \leq 0.46$, the case $R = 0.4$ and $R = 1.0$ both show larger circulation values, whereas when $t/T > 0.46$, the circulation of case $R = 0.0$ is larger than that of the other two cases. The circulation is also calculated on the horizontal planes. Figure 9(b) shows the circulation results calculated at the horizontal slice cross the mid-span of the caudal fin leading edge. Similar to Fig. 9(a), a larger circulation value is first observed for case $R = 0.4$ and $R = 1.0$, and then it falls below $R = 0.0$ case when $t/T > 0.50$. Figure 9(c) shows the time course of the circulation change in another horizontal slice at three-quarters-span of the leading edge. The results indicate that, at this position, the cases $R = 0.0$ and $R = 0.4$ share similar circulation values and only the $R = 1.0$ case has a dorsal fin stretching high enough to make a difference in the caudal fin LEV circulation. The circulation result here echoes the instantaneous force results in Fig. 6(b) and explains why larger caudal fin thrust occurs when $R = 1.0$.

To further examine the thrust enhancement mechanism, cycle-averaged thrust distribution is plotted on the caudal fin in Fig. 10. These plots indicate that, for all three cases, most of the thrust
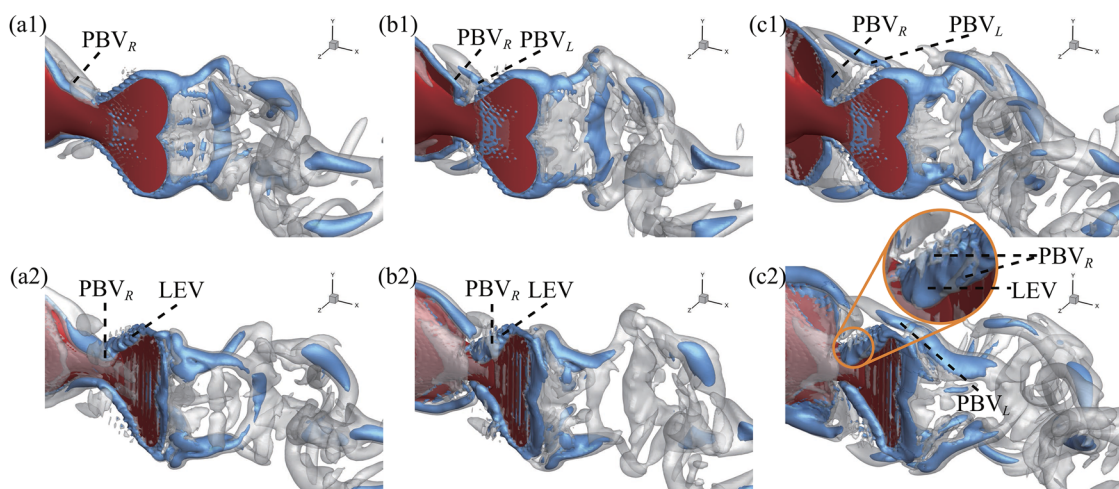

FIG. 7. Three-dimensional wake structures of models with $R = 0.0$ [(a1) and (a2)], $R = 0.4$ [(b1) and (b2)], and $R = 1.0$ [(c1) and (c2)] at $t/T = 0.58$ [(a1), (b1), and (c1)] and $t/T = 0.83$ [(a2), (b2), and (c2)].
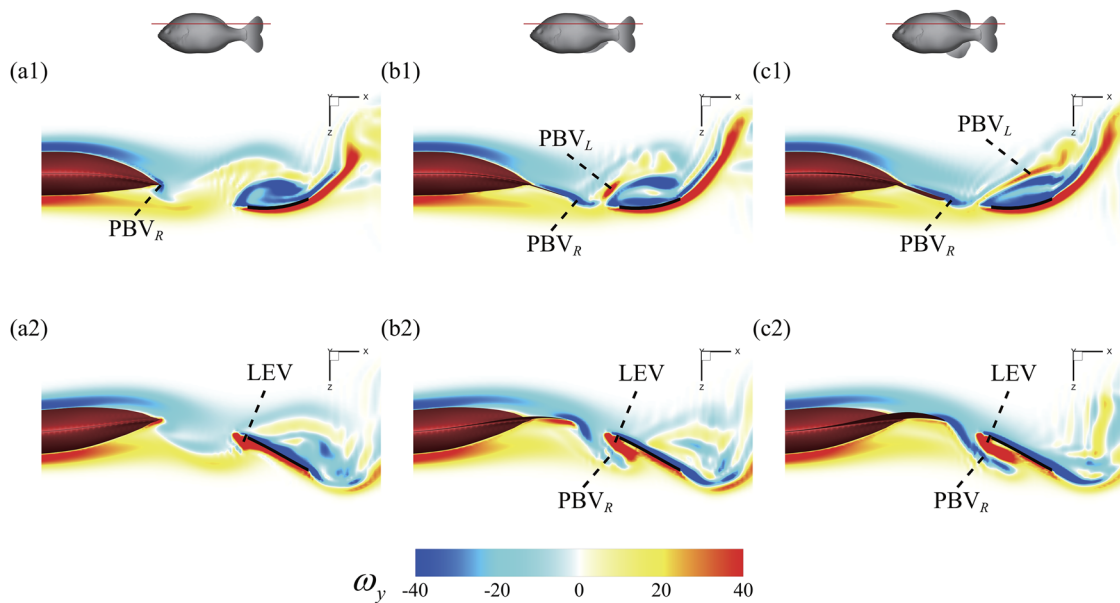
FIG. 8. Contours of ω_y from a horizontal slice, whose position is shown by the red lines on the top of this figure, at $t/T = 0.58$ [(a1), (b1), and (c1)], and $t/T = 0.83$ [(a2), (b2), and (c2)]. [(a1) and (a2)] $R = 0.0$; [(b1) and (b2)] $R = 0.4$; and [(c1) and (c2)] $R = 1.0$.

is generated in the leading-edge region of the caudal fin, which in turn implies that LEV is responsible for caudal fin thrust generation. Compared to the case $R = 0.0$, the dorsal and anal fins in cases $R = 0.4$ and $R = 1.0$ increase the magnitude of cycle-averaged thrust significantly and it is obvious that the mean thrust magnitude of case $R = 0.4$ is between the other two cases, which is consistent with the results in Fig. 6.

In summary, our results in this section show that the interactions between the PBVs generated by the dorsal and anal fins and the LEVs generated by the caudal fin are the main reasons for caudal fin thrust enhancement. Larger dorsal and anal fin area results in a stronger interaction and thus higher caudal fin thrust.

C. Effects of dorsal and anal fin flapping phase

In this section we examine the effects of dorsal and anal fin flapping phase φ on caudal fin hydrodynamic performance when $R = 1.0$, since the phase affects the interaction timing between

median fin vortices and thus is expected to influence propulsive performance of the caudal fin.

Numerical simulations are conducted when the kinematics of trunk and caudal fin remain unchanged, whereas the flapping phase φ of the dorsal and anal fins varies from $-100°$ to $100°$, where the negative value defines phase-leading dorsal and anal fins, and the positive value defines phase-lag dorsal and anal fins. Figure 11(a) shows variations in the cycle-averaged thrust and power coefficients with respect to φ. We found that thrust generated by the caudal fin increases with the increase of φ and reaches its maximum value at $\varphi = 20°$. After that, thrust decreases slightly. Compared to the thrust of the trunk-caudal fin only case ($R = 0.0$), which is denoted by the red dashed line in Fig. 11(a), in the presence of the dorsal and anal fins, in most cases, thrust enhancement can be achieved. For instance, when $\varphi = 20°$, a 26.5% increase in thrust is observed. In Fig. 11(a), the cycle-averaged hydrodynamic power of the caudal fin shares a similar trend with thrust. As the phase difference increases
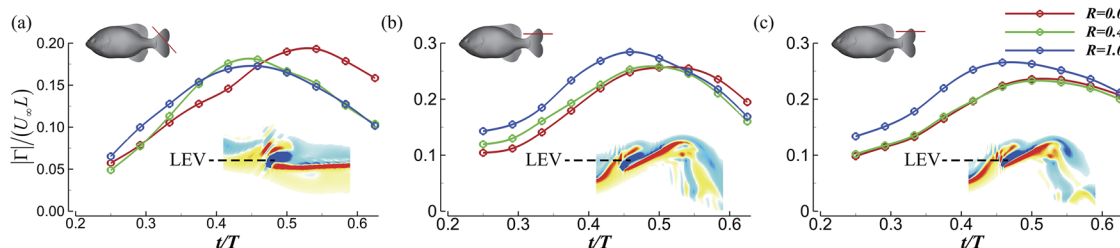

FIG. 9. Caudal fin LEV circulation at (a) a slice, which is perpendicular to the leading edge of the caudal fin at its mid-span, (b) a horizontal slice through the mid-span of the caudal fin leading edge, and (c) a horizontal slice through the three-quarters-span of the caudal fin leading edge. The positions of those slices are shown in the images above the plots.
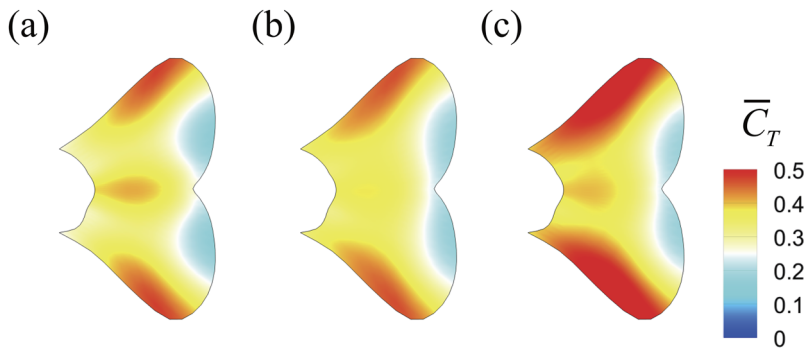
FIG. 10. Distributions of the cycle-averaged thrust $\overline{C}_T$ on the caudal fin. (a) $R = 0.0$, (b) $R = 0.4$, and (c) $R = 1.0$.

from $-100°$ to $0°$, although the power consumption increases substantially, its magnitude is still less than that of the trunk-caudal fin only case, which is denoted by the blue dashed line in Fig. 11(a). As the phase difference increases further, power consumption increases slightly and then reaches a steady state. Efficiency is plotted in Fig. 11(b) with respect to the phase difference. Again, the efficiency of the trunk-caudal fin only case is denoted by a dashed line for direct comparison. The most efficient case occurs at $\varphi = -60°$, and there is a nearly 50% increase in efficiency when compared to the trunk-caudal fin only case. With further increases in phase difference, efficiency begins to decrease. However, even for the largest phase difference $100°$ we studied here, a 9% increase in efficiency is achieved when compared to the trunk-caudal fin only case. These results show that for the dorsal and anal fins flapping out of phase with the caudal fin, a phase lead leads to higher caudal fin efficiency, whereas a phase lag tends to maintain caudal fin thrust at a high level.

To get further insight into the physics of median fin interactions, simulation results of the largest thrust case ($\varphi = 20°$) and the most efficient case ($\varphi = -60°$) are examined. Figure 12 compares instantaneous thrust generation and power consumption for this condition. Due to the symmetry of the kinematics, it is reasonable for us to focus on the first thrust/power maximum only. It is found that, for both cases, the maximum instantaneous thrust happens approximately at $t/T = 0.30$, when the leading edge of the caudal fin is midway during its leftward motion, though for the case $\varphi = 20°$, a small time-delay is observed. Most of the thrust difference happens at this time, until the leading edge of the caudal fin reaches its leftmost position and starts to flap back, which

corresponds to the time instant $t/T = 0.58$ in Fig. 12(a). Power consumption shown in Fig. 12(b) shares a similar trend with thrust generation.

Figure 13 compares the wake structures of these two cases. When the caudal fin is at its mid-position [Figs. 13(a1) and 13(b1)], a LEV is formed. For both cases, PBV_L is shed from the dorsal fin. Later, with the caudal fin flapping leftward as shown in Figs. 13(a2) and 13(b2), the LEV becomes stronger. In Fig. 13(a2), a PBV_L tube can be seen approaching the caudal fin on the right side and colliding with the LEV, whereas in Fig. 13(b2), the corresponding PBV_L structure is observed on the left side of the caudal fin, and thus is unable to interact with the LEV. Plots in Figs. 13(a3) and 13(b3) clearly show the differences between the resultant wake structures of these two cases. In Fig. 13(a3), a strong LEV is observed, whereas in Fig. 13(b3), the LEV is much weaker.

Figure 14 shows the spanwise vorticity contours of the cases $\varphi = 20°$ and $-60°$ at the same time instants as shown in Fig. 13 to demonstrate the effects of the phase difference on the MFI. First, in Figs. 14(a1) and 14(b1), both cases show the existence of a developing LEV. However, the positions of the PBV_L are very different. In Fig. 14(a1), the PBV_L arrives at the leading edge of the caudal fin and starts to interact with the LEV, whereas in Fig. 14(b1), the main part of PBV_L is still at its halfway point. Though a small-scale PBV_L and LEV interaction happens in Fig. 14(b1) at the leading edge of the caudal fin, it is too small to illustrate clearly. In Fig. 14(a2), for case $\varphi = 20°$, the interactions between PBV_L and LEV become more obvious. The PBV_L from dorsal fin shows a tendency to destabilize the LEV and induce the LEV to tilt away from the caudal fin.
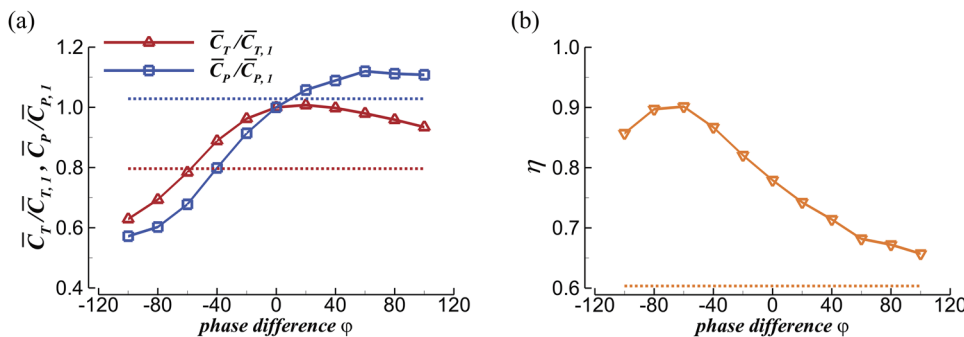

FIG. 11. (a) Cycle-averaged thrust and power coefficients of the caudal fin and (b) efficiency of the caudal fin, for the entire range of phase difference studied. All values in (a) are normalized with respect to the baseline case $R = 1.0$, $\varphi = 0°$. The dashed red and blue lines in (a) and dashed orange line in (b) correspond to the mean thrust coefficient, power coefficient, and efficiency of the trunk-caudal fin only case.
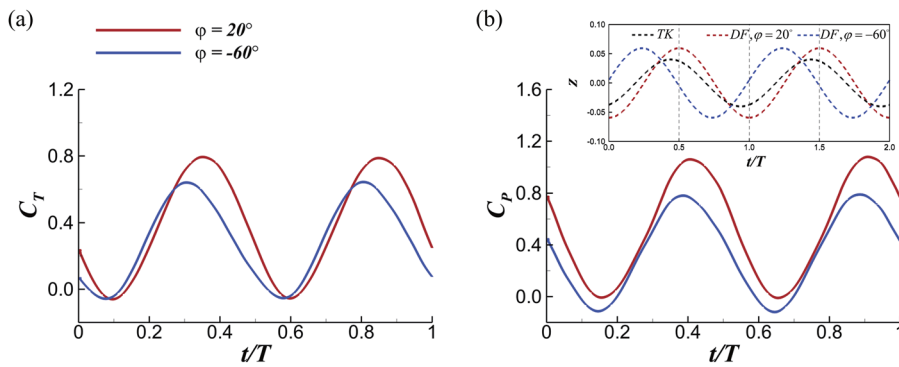
FIG. 12. (a) Caudal fin thrust coefficients and (b) caudal fin power coefficients for cases with phase differences $\varphi = 20°$ and $\varphi = −60°$ during one representative tail beat. At the top right corner, the lateral excursions of the trunk dorsal edge and dorsal fin outer edge are plotted for these two cases at $x/L = 0.70$ to show the kinematics difference.

However, at the same time instant, instead of interacting with the caudal fin, the main part of PBV_L in Fig. 14(b2) travels to the left side of the caudal fin. Figures 14(a3) and 14(b3) show the comparison between the resultant vorticity structures of these two cases. In Fig. 14(a3), a noticeable LEV is observed separating from the leading edge of the caudal fin and then recoiling toward the trailing edge of the caudal fin. In Fig. 14(b3), due to the phase difference, the above-mentioned interactions are not observed. Although an LEV can still be seen in Fig. 14(b3) attaching to the leading edge of the caudal fin, its strength is much weaker than the LEV in Fig. 14(a3).

Figure 15 shows the cycle-averaged thrust distributions on the caudal fin in these two cases. The thrust of case $\varphi = 20°$ is much larger than that of case $\varphi = −60°$ in magnitude, especially at the leading edge and dorsal and ventral tips of the caudal fin, where the PBVs and the LEVs interact the most as shown in Fig. 14. In addition, corresponding to the LEV recoil in Fig. 14(a3), thrust at the caudal fin trailing edge is also larger for case $\varphi = 20°$. From Fig. 15, it is also noticed that, compared to the thrust distribution of case $\varphi = 20°$, the $\varphi = −60°$ case shows a more asymmetric pattern. Comparisons between the geometries of the dorsal and anal fins in

Fig. 1(a) show that there is a concave at the posterior outer edge of the anal fin. With this concave, the streamwise distance between the anal fin trailing edge and caudal fin leading edge is larger than that of the dorsal fin. At $\varphi = −60°$, the difference in the streamwise distance between dorsal/anal fin and caudal fin produces larger asymmetric thrust distribution on the dorsal and ventral lobes of the caudal fin.

D. Effects of dorsal and anal fins on trunk drag

In this section, the effects of the dorsal and anal fins on the hydrodynamic performance of the fish trunk are investigated by changing the shape and flapping phase of these two fins. Figure 16(a) shows a plot of cycle-averaged drag and power coefficients ($\overline{C}_{D,Trunk}$ and $\overline{C}_{P,Trunk}$) of the body trunk region vs the shape factor. Compared to the trunk-caudal fin only case ($R = 0.0$), which implies completely folded dorsal and anal fins, low height of the dorsal and anal fins ($R = 0.2$) can reduce trunk drag by 8.3% and trunk power by 3.4%. Furthermore, the increase in the dorsal and anal fin area reduces the trunk drag further, though the power consumption is increased slightly. When $R = 1.0$, the drag force on the trunk is observed to be reduced by 15.2%, whereas the power consumption
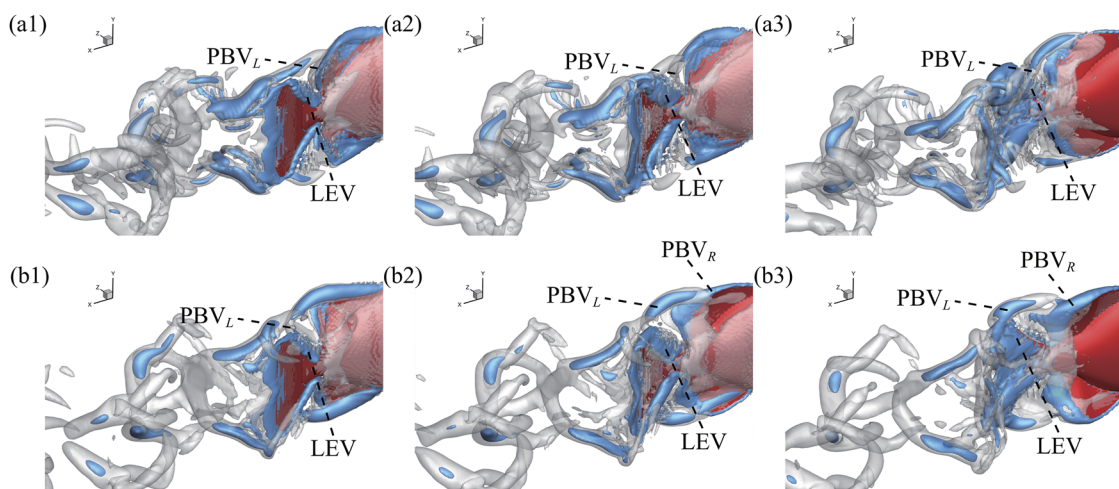

FIG. 13. Three-dimensional wake structures of models with $\varphi = 20°$ [(a1), (a2), and (a3)] and $\varphi = −60°$ [(b1), (b2), and (b3)] at $t/T = 0.30$ [(a1) and (b1)]; $t/T = 0.42$ [(a2) and (b2)] and $t/T = 0.58$ [(a3) and (b3)].
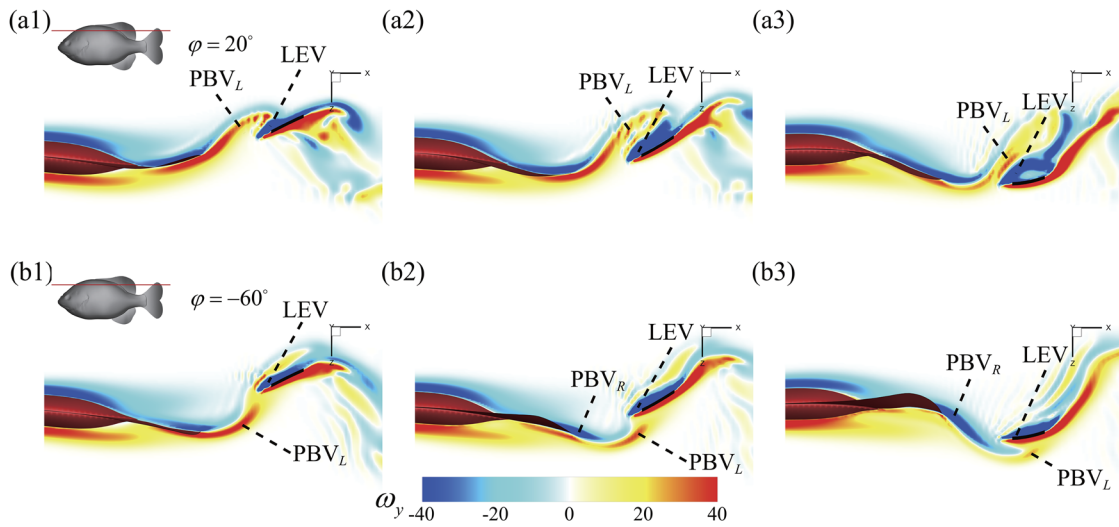
FIG. 14. Contours of ω_y on a horizontal slice, whose position is shown by the red lines on the top of this figure, at $t/T = 0.30$ [(a1) and (b1)]; $t/T = 0.42$ [(a2) and (b2)] and $t/T = 0.58$ [(a3) and (b3)]. [(a1), (a2), and (a3)] $\varphi = 20°$ and [(b1), (b2), and (b3)] $\varphi = -60°$.

is increased by merely 4.1%, which still indicates a remarkable performance enhancement. Noticeably, when $R > 1.0$, increasing the dorsal and anal fin area only reduces the trunk drag marginally, whereas the power consumption continues to increase. From $R = 1.0$ to $R = 1.4$, $\overline{C}_{D,Trunk}$ is reduced by only 0.5%, whereas $\overline{C}_{P,Trunk}$ is increased by 3.8%, which suggests that benefits from dorsal/anal fin erection do not occur at all parameter combinations. Expanding the fins too much means paying a larger power penalty for a small reduction in the trunk drag, which is not optimal.

To look further into the drag reduction on the trunk, in Fig. 16(b), the instantaneous trunk drag of models with different dorsal/anal fin shapes is plotted. Consistent with the results shown in Fig. 16(a) and Fig. 16(b), larger dorsal and anal fins correspond to smaller trunk drag magnitudes. We also observe that the case $R = 0.4$ presents the smallest peak-to-peak trunk drag force fluctuation, whereas $R = 0.0$ shows the largest. With the increase in dorsal and anal fin area, in addition to the reducing drag force magnitude, the phase of the instantaneous trunk drag is also changed. For example, in Fig. 16(b), the trunk drag of cases $R = 1.0$ and 1.4 are out of phase with that of the trunk-caudal fin only case.

In Fig. 17, the body surface pressure distributions of different cases are compared, where the pressure coefficient $\tilde{p}$ is defined as $\tilde{p} = (p - p_\infty)/0.5\rho U_\infty^2$ and p_∞ is the pressure in the free stream. The comparison is made at $t/T = 0.58$, when the largest drag difference happens in Fig. 16(b). From Fig. 17, no obvious difference can be observed at the anterior part of trunk. However, at the posterior region of the trunk, compared to the $R = 0.0$ case, with the presence of the dorsal and anal fins, in Figs. 17(b1) and 17(c1) a lower-pressure suction zone is found on the left side of the trunk, and in Figs. 17(b2) and 17(c2), a higher-pressure pressure zone is found on the right side. Thus, the larger dorsal/anal fin area is responsible for the generation of a lower-pressure suction zone and higher-pressure pressure zone.

To investigate the causes of the differences in trunk pressure distributions between these cases, in Fig. 18, two vertical slices are cut in the flow field at the locations where the trunk pressure difference is the highest. In these three cases, at $t/T = 0.58$, PBVs can be seen shedding from the outer edges of the posterior body part, though only dorsal edge shedding PBVs are denoted in Fig. 18 for clarity. We note that, for case $R = 0.0$, in Fig. 18(a), when the corresponding trunk region finishes its leftward flapping stroke and starts to move back, the PBV_R generated from the last rightward flapping stroke rolls over the round dorsal edge of the trunk and interacts with the newly generated PBV_L at the right side of the trunk. However, the interaction here is detrimental to the formation of a
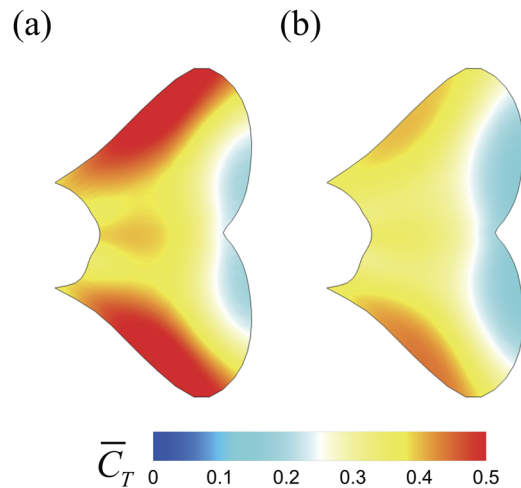

FIG. 15. Distributions of the cycle-averaged thrust $\overline{C}_T$ on the caudal fin. (a) $\varphi = 20°$ and (b) $\varphi = -60°$.
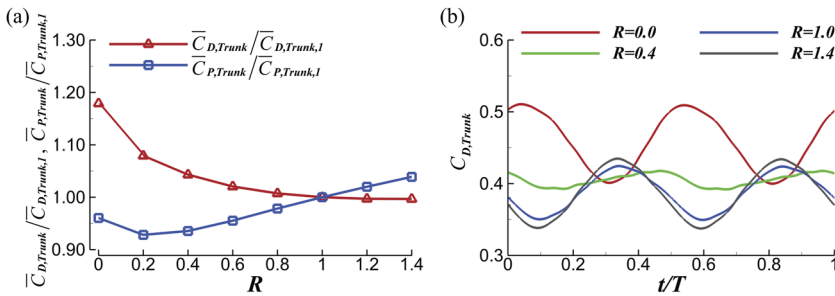
FIG. 16. (a) Cycle-averaged trunk drag $\left(\overline{C}_{D,Trunk}\right)$ and power coefficients $\left(\overline{C}_{P,Trunk}\right)$ corresponding to different dorsal/anal fin shapes. All values are normalized with respect to the baseline case $R = 1.0$ and $\varphi = 0°$. (b) Instantaneous trunk drag of models with different dorsal/anal fin shapes during one representative tail beat.

higher-pressure zone. Meanwhile, in Fig. 18(c), due to the presence of the dorsal fin, the PBV$_R$ is blocked and prevented from shifting to the right side of the trunk. On the other hand, in Fig. 18(c), the major part of the PBV$_L$ is still attached to the outer edge of the dorsal fin. Thus, in contrast to what is shown in Fig. 18(a), in Fig. 18(c), the interaction between the PBV$_R$ and PBV$_L$ does not happen near the trunk region, and this leads to the higher-pressure pressure zone shown in Fig. 17(c2). Wake structures of case $R = 0.4$ are also plotted in Fig. 18(b) to facilitate a direct comparison. The PBV$_R$ in Fig. 18(b) is weaker when compared to the condition shown in Fig. 18(a). As a result, a moderate high-pressure region is generated and seen in Fig. 17(b2), and the body drag force of case $R = 0.4$ is thus between the other two cases in magnitude.

In the previous study of jack fish swimming by Liu *et al.*,[10] a similar amount of trunk drag reduction was also reported due to the presence of dorsal and anal fins. In that paper drag reduction was attributed to an edge vortex propulsion mechanism, which is consistent with that observed for fish larvae.[44] However, in this paper, the results show that, instead of merely generating edge vortices, the presence of the dorsal and anal fins can prevent the PBVs from transferring to the opposite side of the trunk and thus weaken

the interactions between PBV$_R$ and PBV$_L$ near the trunk region to reduce the trunk drag.

Furthermore, we examine the effects of the dorsal/anal fin flapping phase on the hydrodynamic performance of the trunk region, and we plot the results in Fig. 19. Figure 19(a) shows that the cycle-averaged drag on the trunk is at its maximum value when $\varphi = 100°$, which is the largest phase difference we studied here. However, in this case, the trunk drag is still smaller than that of the trunk-caudal fin only case, which is denoted by the red dashed line in Fig. 19(a). As the phase difference decreases, drag on the trunk decreases, whereas the power consumption of the trunk increases a small amount and then reduces. When φ goes to $-40°$, although the power consumed by the trunk is of nearly the same magnitude as that of the trunk-caudal fin only case, which is denoted by the blue dashed line in Fig. 19(a), trunk drag shows a 22.2% reduction. Figure 19(b) compares the instantaneous trunk drag among models with different dorsal/anal fin flapping phases. We observe that, with dorsal/anal fin phase changes, the phase of the trunk drag in Fig. 19(b) also changes significantly. As φ increases, the peaks and troughs of the trunk drag are delayed by a certain phase. Also, in Fig. 19(b), when $\varphi \leq 0°$, which implies dorsal/anal fins lead the caudal fin, although
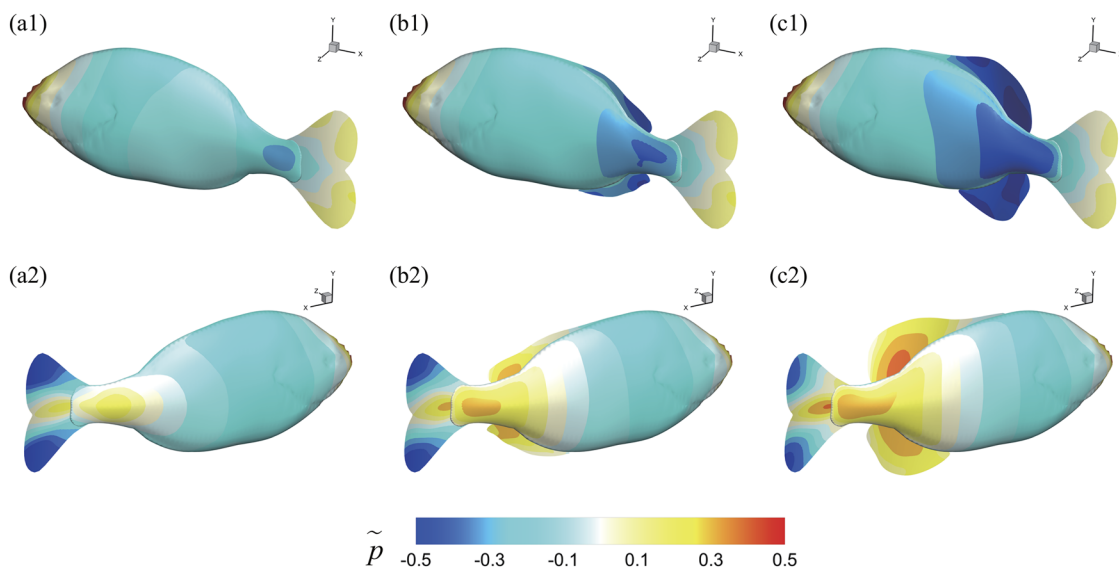

FIG. 17. Surface pressure of cases $R = 0.0$ [(a1) and (a2)], $R = 0.4$ [(b1) and (b2)], and $R = 1.0$ [(c1) and (c2)] at $t/T = 0.58$. (a1), (b1), and (c1) show the left side of the fish model, and (a2), (b2), and (c2) show the right side.
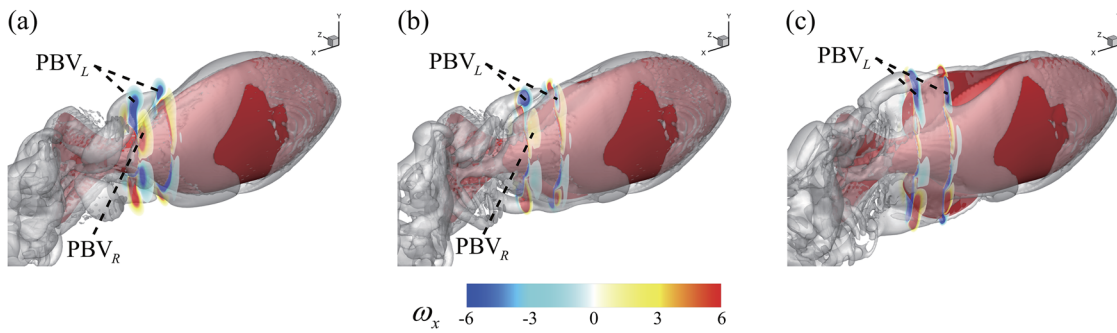
FIG. 18. Three-dimensional wake structures ($Q = 0.5$) and contours of ω_x on two vertical slices cutting through the flow field at $t/T = 0.58$. (a) $R = 0.0$, (b) $R = 0.4$, and (c) $R = 1.0$.
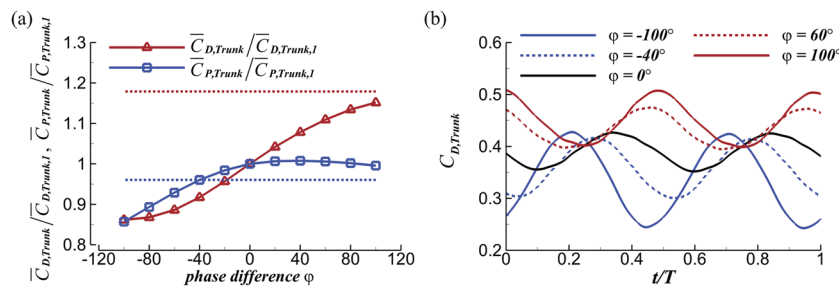

FIG. 19. (a) Cycle-averaged trunk drag ($\overline{C}_{D,Trunk}$) and power coefficients ($\overline{C}_{P,Trunk}$) corresponding to different dorsal/anal fin flapping phases. All values are normalized with respect to the baseline case $R = 1.0$, $\varphi = 0°$. The dashed red and blue lines denote the cycle-averaged trunk drag and power coefficients of the trunk-caudal fin only case. (b) Instantaneous trunk drag of models with different dorsal/anal fin flapping phases during one representative tail beat.

substantial trunk drag reduction occurs, the magnitude of the drag peak does not change substantially. However, if we look at the trough values, compared to the case $\varphi = 0°$, up to 30% magnitude reduction can be observed when $\varphi = -100°$. When $\varphi > 0°$, the reverse trend is observed.

In summary, the results of this section demonstrate that, by reducing the interactions between the PBV_L and PBV_R, the dorsal and anal fins can induce a higher-pressure pressure zone and lower-pressure suction zone on the opposite sides of the trunk. This enhanced pressure difference is proposed to reduce the trunk drag. We also show that changing the flapping phase of the dorsal and anal fins can further reduce the trunk drag. In this study, when $R = 1.0$ and $\varphi = -40°$, as much as 22.2% of the trunk drag can be reduced compared to the trunk-caudal fin only case.

V. CONCLUSION

Using a carangiform swimmer model of bluegill sunfish, 3D numerical simulations are conducted to explore the effects of the dorsal/anal fin shape and flapping phase on the hydrodynamic performance and associated vortex dynamics in fish-like swimming, with the aim of investigating the benefits of dorsal and anal fins as control surfaces independent of the caudal fin.

Investigations into the dorsal and anal fin shape effects show that, by generating stronger PBVs, larger dorsal and anal fins induce stronger caudal fin LEVs and thus produce higher caudal fin thrust and efficiency. Numerical simulations also reveal that the dorsal/anal

fin phase lag and lead are related to higher caudal fin thrust and efficiency, respectively. By utilizing the appropriate flapping phase, a 26.5% increase in thrust or a 50% increase in efficiency can be achieved when compared to the trunk-caudal fin only case. This is attributed to the alteration of the interaction timing of vortices shed by the dorsal and anal fins and the caudal fin. With an appropriate phase lag, PBVs interact with the LEV and thus give rise to a higher thrust. However, a leading-edge vortex separation is observed later at this fin phase, which results in lower efficiency, when compared to the phase lead case. With the dorsal and anal fins leading the trunk phase by $60°$, the propulsive performance of the caudal fin is improved to 90.1%, when the trunk-caudal fin only case shows an efficiency of 60.3%.

Besides caudal fin performance enhancement, this study also demonstrates the effects of the dorsal/anal fin shape and flapping phase on drag of the body/trunk region. When dorsal and anal fins are present, PBVs are prevented from transferring across the edge of the body trunk. The interactions between the PBV_L and PBV_R are thus inhibited and a larger pressure difference is created between the two sides of the body trunk. As the body undulates in swimming, this larger pressure difference produces a reduction in the trunk drag. Simulation results show that, compared to the trunk-caudal fin only case, the baseline case here ($R = 1.0$, $\varphi = 0°$) reduces the trunk drag by about 15.2% with a mere 4.1% increase in the trunk power consumption. The flapping phase of the dorsal and anal fins is also found to be crucial to trunk drag reduction. With a dorsal/anal fin phase lead of $40°$, compared to the trunk-caudal fin only case, trunk drag can

be reduced by as much as 22.2% while a similar amount of power is consumed.

ACKNOWLEDGMENTS

REFERENCES

[1]M. Sfakiotakis, D. M. Lane, and J. B. C. Davies, "Review of fish swimming modes for aquatic locomotion," IEEE J. Oceanic Eng. **24**, 237 (1999).

[2]G. V. Lauder and E. G. Drucker, "Morphology and experimental hydrodynamics of fish fin control surfaces," IEEE J. Oceanic Eng. **29**, 556 (2004).

[3]M. Lighthill, "Aquatic animal propulsion of high hydromechanical efficiency," J. Fluid Mech. **44**, 265 (1970).

[4]D. Weihs, "Design features and mechanics of axial locomotion in fish," Am. Zool. **29**, 151 (1989).

[5]M. Wolfgang, J. Anderson, M. Grosenbaugh, D. Yue, and M. Triantafyllou, "Near-body flow dynamics in swimming fish," J. Exp. Biol. **202**, 2303 (1999).

[6]E. G. Drucker and G. V. Lauder, "Locomotor function of the dorsal fin in teleost fishes: Experimental analysis of wake forces in sunfish," J. Exp. Biol. **204**, 2943 (2001).

[7]E. G. Drucker and G. V. Lauder, "Locomotor function of the dorsal fin in rainbow trout: Kinematic patterns and hydrodynamic forces," J. Exp. Biol. **208**, 4479 (2005).

[8]E. D. Tytell, "Median fin function in bluegill sunfish *Lepomis macrochirus*: Streamwise vortex structure during steady swimming," J. Exp. Biol. **209**, 1516 (2006).

[9]E. Standen and G. V. Lauder, "Hydrodynamic function of dorsal and anal fins in brook trout (*Salvelinus fontinalis*)," J. Exp. Biol. **210**, 325 (2007).

[10]G. Liu, Y. Ren, H. Dong, O. Akanyeti, J. C. Liao, and G. V. Lauder, "Computational analysis of vortex dynamics and performance enhancement due to body–fin and fin–fin interactions in fish-like locomotion," J. Fluid Mech. **829**, 65 (2017).

[11]I. Borazjani and M. Daghooghi, "The fish tail motion forms an attached leading edge vortex," Proc. R. Soc. B **280**, 20122071 (2013).

[12]Q. Zhong, H. Dong, and D. B. Quinn, "How dorsal fin sharpness affects swimming speed and economy," J. Fluid Mech. **878**, 370 (2019).

[13]P. Geerlink and J. Videler, "Joints and muscles of the dorsal fin of Tilapia nilotica L. (Fam. Cichlidae)," Neth. J. Zool. **24**, 279 (1973).

[14]L. Wen, Z. Ren, V. Di Santo, K. Hu, T. Yuan, T. Wang, and G. V. Lauder, "Understanding fish linear acceleration using an undulatory biorobotic model with soft fluidic elastomer actuated morphing median fins," Soft Rob. **5**, 375 (2018).

[15]E. D. Tytell, E. M. Standen, and G. V. Lauder, "Escaping Flatland: Three-dimensional kinematics and hydrodynamics of median fins in fishes," J. Exp. Biol. **211**, 187 (2008).

[16]E. Standen and G. V. Lauder, "Dorsal and anal fin function in bluegill sunfish *Lepomis macrochirus*: Three-dimensional kinematics during propulsion and maneuvering," J. Exp. Biol. **208**, 2753 (2005).

[17]A. MacLean, N. B. Metcalfe, and D. Mitchell, "Alternative competitive strategies in juvenile Atlantic salmon (*Salmo salar*): Evidence from fin damage," Aquaculture **184**, 291 (2000).

[18]I. Hoyle, B. Oidtmann, T. Ellis, J. Turnbull, B. North, J. Nikolaidis, and T. G. Knowles, "A validated macroscopic key to assess fin damage in farmed rainbow trout (*Oncorhynchus mykiss*)," Aquaculture **270**, 142 (2007).

[19]J. Person-Le Ruyet, N. Le Bayon, and S. Gros, "How to assess fin damage in rainbow trout, *Oncorhynchus mykiss*?," Aquat. Living Resour. **20**, 191 (2007).

[20]I. Akhtar, R. Mittal, G. V. Lauder, and E. Drucker, "Hydrodynamics of a biologically inspired tandem flapping foil configuration," Theor. Comput. Fluid Dyn. **21**, 155 (2007).

[21]G.-J. Dong and X.-Y. Lu, "Characteristics of flow over traveling wavy foils in a side-by-side arrangement," Phys. Fluids **19**, 057107 (2007).

[22]B. M. Boschitsch, P. A. Dewey, and A. J. Smits, "Propulsive performance of unsteady tandem hydrofoils in an in-line configuration," Phys. Fluids **26**, 051901 (2014).

[23]Y. Bao and J. Tao, "Dynamic reactions of a free-pitching foil to the reverse Kármán vortices," Phys. Fluids **26**, 031704 (2014).

[24]K. Lua, H. Lu, X. Zhang, T. Lim, and K. Yeo, "Aerodynamics of two-dimensional flapping wings in tandem configuration," Phys. Fluids **28**, 121901 (2016).

[25]G. Xu, W. Duan, and W. Xu, "The propulsion of two flapping foils with tandem configuration and vortex interactions," Phys. Fluids **29**, 097102 (2017).

[26]M. S. U. Khalid, I. Akhtar, H. Imtiaz, H. Dong, and B. Wu, "On the hydrodynamics and nonlinear interaction between fish in tandem configuration," Ocean Eng. **157**, 108 (2018).

[27]M. Saadat, F. E. Fish, A. Domel, V. Di Santo, G. Lauder, and H. Haj-Hariri, "On the rules for aquatic locomotion," Phys. Rev. Fluids **2**, 083102 (2017).

[28]A. Maia, G. V. Lauder, and C. D. Wilga, "Hydrodynamic function of dorsal fins in spiny dogfish and bamboo sharks during steady swimming," J. Exp. Biol. **220**, 3967 (2017).

[29]C. Li, and H. Dong, "Wing kinematics measurement and aerodynamics of a dragonfly in turning flight," Bioinspiration Biomimetics **12**, 026001 (2017).

[30]I. Borazjani and F. Sotiropoulos, "Numerical investigation of the hydrodynamics of carangiform swimming in the transitional and inertial flow regimes," J. Exp. Biol. **211**, 1541 (2008).

[31]C. Lindsey, "Form, function and locomotory habits in fish," in *Locomotion*, Fish Physiology Vol. 7 (Elsevier, 1978), pp. 1–100.

[32]E. D. Tytell, "The hydrodynamics of eel swimming II. Effect of swimming speed," J. Exp. Biol. **207**, 3265 (2004).

[33]B. C. Jayne and G. V. Lauder, "Speed effects on midline kinematics during steady undulatory swimming of largemouth bass, Micropterus salmoides," J. Exp. Biol. **198**, 585 (1995).

[34]J. Long, M. McHenry, and N. Boetticher, "Undulatory swimming: How traveling waves are produced and modulated in sunfish (*Lepomis gibbosus*)," J. Exp. Biol. **192**, 129 (1994).

[35]J. Videler and C. Wardle, "Fish swimming stride by stride: Speed limits and endurance," Rev. Fish Biol. Fish. **1**, 23 (1991).

[36]G. S. Triantafyllou, M. Triantafyllou, and M. Grosenbaugh, "Optimal thrust development in oscillating foils with application to fish propulsion," J. Fluids Struct. **7**, 205 (1993).

[37]J. Anderson, K. Streitlien, D. Barrett, and M. Triantafyllou, "Oscillating foils of high propulsive efficiency," J. Fluid Mech. **360**, 41 (1998).

[38]H. Dong, R. Mittal, M. Bozkurttas, R. Mittal, P. Madden, and G. Lauder, "Computational modelling and analysis of the hydrodynamics of a highly deformable fish pectoral fin," J. Fluid Mech. **645**, 345 (2010).

[39]G. Liu, Y. Ren, J. Zhu, H. Bart-Smith, and H. Dong, "Thrust producing mechanisms in ray-inspired underwater vehicle propulsion," Theor. Appl. Mech. Lett. **5**, 54 (2015).

[40]Z. Liang and H. Dong, "On the symmetry of proper orthogonal decomposition modes of a low-aspect-ratio plate," Phys. Fluids **27**, 063601 (2015).

[41]C. Li and H. Dong, "Three-dimensional wake topology and propulsive performance of low-aspect-ratio pitching-rolling plates," Phys. Fluids **28**, 071901 (2016).

[42]H. Dong, R. Mittal, and F. Najjar, "Wake topology and hydrodynamic performance of low-aspect-ratio flapping foils," J. Fluid Mech. **566**, 309 (2006).

[43]C. Li, H. Dong, and G. Liu, "Effects of a dynamic trailing-edge flap on the aerodynamic performance and flow structures in hovering flight," J. Fluids Struct. **58**, 49 (2015).

[44]G. Li, U. K. Müller, J. L. van Leeuwen, and H. Liu, "Fish larvae exploit edge vortices along their dorsal and ventral fin folds to propel themselves," J. R. Soc., Interface **13**, 20160068 (2016).